MATERIALS SCIENCE

A new mechanism for void-cascade interaction from nondestructive depth-resolved atomic-scale measurements of ion irradiation–induced defects in Fe

S. Agarwal[1,2], M. O. Liedke[3], A. C. L. Jones[1,2], E. Reed[2], A. A. Kohnert[4], B. P. Uberuaga[4]*, Y. Q. Wang[4], J. Cooper[5], D. Kaoumi[5], N. Li[6], R. Auguste[7], P. Hosemann[7], L. Capolungo[4], D. J. Edwards[8], M. Butterling[3], E. Hirschmann[3], A. Wagner[3], F. A. Selim[1,2]*

The nondestructive investigation of single vacancies and vacancy clusters in ion-irradiated samples requires a depth-resolved probe with atomic sensitivity to defects. The recent development of short-pulsed positron beams provides such a probe. Here, we combine depth-resolved Doppler broadening and positron annihilation lifetime spectroscopies to identify vacancy clusters in ion-irradiated Fe and measure their density as a function of depth. Despite large concentrations of dislocations and voids in the pristine samples, positron annihilation measurements uncovered the structure of vacancy clusters and the change in their size and density with irradiation dose. When combined with transmission electron microscopy measurements, the study demonstrates an association between the increase in the density of small vacancy clusters with irradiation and a remarkable reduction in the size of large voids. This, previously unknown, mechanism for the interaction of cascade damage with voids in ion-irradiated materials is a consequence of the high porosity of the initial microstructure.

INTRODUCTION

Radiation damage is a research topic of high importance, affecting many major areas of science (*1*–*6*). Much of that research has focused on the interaction of high-energy particles with materials (*2*, *3*, *7*), with previous studies revealing the formation of a wide range of defect types such as interstitials, dislocation loops, vacancies, and voids (*8*). These defects can cause detrimental changes in properties including swelling, hardening, and embrittlement (*9*) and are expected to affect how the material reacts to other environments, such as a corrosive medium. Thus, it is critical to understand the nature of these defects and their properties on the atomistic scale. Despite the large number of studies on radiation damage in materials, there is still much that is unknown about how defects are generated at the atomic scale and how those defects interact with the preexisting microstructure. Much of what is known comes from atomistic simulations, which, while valuable, always have substantial uncertainties. Thus, fundamental insights into the damage produced in materials can aid in developing models of damage evolution. While destructive microscopy and imaging techniques such as high-resolution transmission electron microscopy (HR-TEM) have provided invaluable information regarding irradiation-induced voids and loops, they cannot capture defects on the atomic scale, such as single vacancies or small clusters less than 1.5 nm in size. Nuclear probes such as positron annihilation lifetime spectroscopy (PALS) have been used to provide quantitative information regarding the size, type, and density of single vacancies and small vacancy clusters for many decades (*10*–*12*). However, this technique has been limited to probing defects in bulk materials because of the absence of depth-resolved positron probes with the timing resolution essential for PALS (*13*). This has traditionally made PALS a technique incompatible with the study of ion beam–irradiated materials.

While ion beams afford several advantages over neutron irradiations, including speed, control, and systematic variation, that are attractive for fundamental studies, they also have notable limitations. Ion irradiation results in a nonuniform damage profile, with the bulk of the damage produced within micrometers of the surface, requiring a depth-resolved probe with atomic-scale sensitivity. Variable energy positron annihilation spectroscopy (VEPAS) has emerged as a reliable tool for such measurements (*14*–*18*). Positrons are accelerated to desired energies and implanted at different depths, where they thermalize and diffuse until they annihilate with an electron, giving rise to two characteristic γ photons of 511 keV, which provide information about the nature and size of defects. While positron studies in the context of slow positron Doppler broadening spectroscopy (DBS), which uses monoenergetic continuous DC positron beams with no timing requirements, have been widely used to profile the overall damage and chemical surrounding of defects that act as positron traps (*19*–*29*), they do not reveal details about the nature and size of individual traps. To reveal such detail, it is imperative to determine the lifetime that positrons spend in the material before annihilation. This requires a birth signal registering the entrance of a positron into the medium and an end signal registering its annihilation, which demands a sophisticated pulsing system.

The realization of this setup is technically challenging, and currently, only a handful of facilities have developed such capabilities (*19*–*21*). To the best of our knowledge, there are only a few studies using PAS to study ion-induced damage, but these either focused on helium implantation (*22*–*24*) or used a destructive sequenced etching technique (*25*). There is no study to date reporting the use of

[1]Center for Photochemical Sciences, Bowling Green State University, Bowling Green, OH 43403, USA. [2]Department of Physics and Astronomy, Bowling Green State University, Bowling Green, OH 43403, USA. [3]Institute of Radiation Physics, Helmholtz-Zentrum Dresden-Rossendorf, Bautzner Landstr. 400, 01328 Dresden, Germany. [4]Materials Science and Technology Division, Los Alamos National Laboratory, Los Alamos, NM 87545, USA. [5]Department of Nuclear Engineering, North Carolina State University, Raleigh, NC 27607, USA. [6]Center for Integrated Nanotechnologies, Materials Physics and Applications Division, Los Alamos National Laboratory, Los Alamos, NM 87545, USA. [7]Department of Nuclear Engineering, University of California, Berkeley, Berkeley, CA 94720, USA. [8]Nuclear Sciences Division, Pacific Northwest National Laboratory, Richland, WA 99352, USA.
*Corresponding author. Email: blas@lanl.gov (B.P.U.); faselim@bgsu.edu (F.A.S.)

nondestructive depth-resolved PALS beam to probe the damage profile in ion-irradiated metallic systems. The current study takes advantage of the newly developed short pulsed positron beam in Dresden, Germany and presents a detailed quantitative assessment for the depth dependence of the damage profile for ion irradiation, capturing both the size and density of vacancy clusters. It highlights the nondestructive nature of this analysis to describe the atomic-scale damage profile of ion irradiation even in highly defected films. By combining PAS with TEM to capture both small clusters and voids/cavities, a novel mechanism for cascade-void interaction in ion-irradiated materials was revealed.

RESULTS AND DISCUSSION

Characterization of reference films by TEM

This study focuses on the defects produced during ion beam irradiation in thin films of Fe. TEM images of the pristine film presented in Fig. 1 show 0.9-μm-thick films with high densities of dislocations and voids. These micrographs reveal that the pristine films, deposited on a Si substrate, contain weakly textured polycrystalline grains about 230 nm in diameter. The dislocation density is estimated to be about $1.5 \times 10^{14}/m^2$. There is also a high degree of porosity/voids in the films. All these features will modify the behavior of positrons in the material, complicating the analysis of the positron spectra. Moreover, they will also modify the propagation of cascades and defects formed during irradiation.

Radiation damage and positron stopping profiles

Figure 2A is a schematic illustrating the range of Fe ions in the films, the induced damage profile, and the implantation of positrons. Figure 2B displays the radiation damage accumulation profile in terms of displacements per atom (dpa), as generated by the SRIM code, when irradiated by 2-MeV Fe ions to a fluence of 5.65×10^{14} ions/cm^2. As expected, the damage profile is nonuniform over the irradiation depth, increasing almost linearly from the surface to the peak dpa region, after which it quickly falls off. In this study, two different fluences are considered, corresponding to peak dpa values of 0.006 and 0.06.

Figure 2C illustrates the intersection of radiation damage profiles with positron stopping profiles at positron implantation energies of 4 and 16 keV (*26*). It is clear that the overlap between the radiation damage curve and positron implantation profile significantly increases with increasing positron incident energy, thus leading to a greater sensitivity of probing damage using positrons at higher average depths. At an implantation energy of 16 keV, the overlap encompasses the complete range of radiation damage as shown in Fig. 2C.

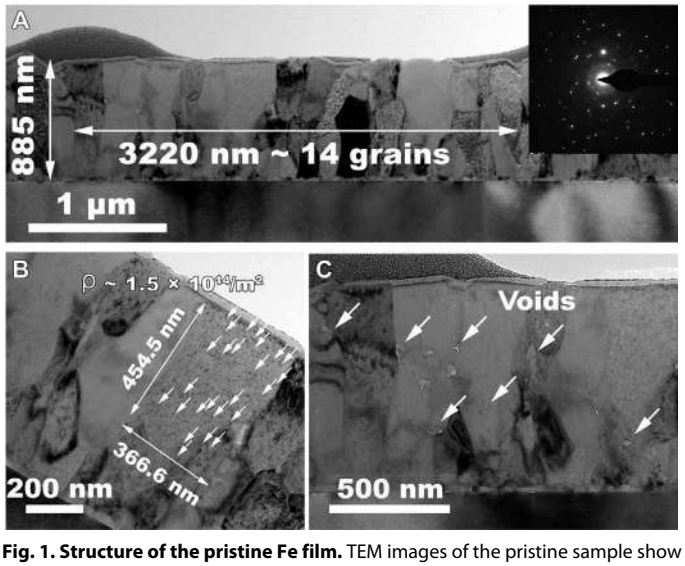

Fig. 1. Structure of the pristine Fe film. TEM images of the pristine sample show (**A**) thickness of the film grown on a Si substrate with an average grain size of ~230 nm, (**B**) dislocation density obtained in the highlighted cross-sectional average grain size, and (**C**) presence of voids throughout the film. The high densities of dislocations and voids indicate that the pristine films are highly defective.

Defect measurements by PAS

The detection of defects by positrons is based on the fact that positrons can be trapped by lattice defects (*27*, *28*). This is because a positron is strongly repelled by ion cores in the lattice as a result of their positive charge; thus, the absence of a positive charge in a vacancy provides an attractive potential that traps positrons at this site. A typical trap site binds the positron with energy on the order of 1 eV, large enough for the thermalized positron to remain trapped until it annihilates.

In DBS, the energy distribution of the positron-electron annihilation radiation is measured; if the electron is moving toward a detector, the detected γ-ray energy is increased through the Doppler shift (*11*). Thus, this method probes the momentum distribution of electrons in solids. As a consequence of positron trapping at defects, the positron wave function primarily overlaps with the wave function of the valence electrons of the surrounding atoms, leading to less Doppler broadening in the annihilation peak. Thus, high-resolution energy measurements of the 511-keV photons can be used to determine the increase in the fraction of positrons annihilated by valence electrons as a result of defects. The increase can be evaluated from the line-shape parameter of the 511-keV peak (the so-called *S* parameter) (*20*–*22*). In PALS, we measure the difference between the time of a positron entering the medium and the time of annihilation, marked by detection of one of the 511-keV photons. While this gives the lifetime of a single positron, a spectrum is typically collected over a period of time. Both DBS and PALS have been used in this study.

Doppler broadening measurements

Figure 3A shows the DBS measurements $S(E)$ for the pristine film and the two irradiated (0.006 and 0.06 dpa) films. Dashed lines represent the fitting of $S(E)$ profiles obtained using VEPFIT (*29*). The defect parameter *S* is sensitive to both the size and concentration of defects and is represented on the vertical axis as a function of positron implantation energy (bottom axis) and corresponding mean penetration depth of positrons (top axis) $\bar{x}$.

A large difference in the shape of the *S* parameter curve between the irradiated and pristine films can be observed in Fig. 3A. In the pristine case, *S* is higher at shallow depths because of the effect of surface states and positronium formation and then decays with depth and starts to plateau at about 190 nm. In the irradiated materials, *S* exhibits the opposite behavior, increasing with depth due to the increase of irradiation-induced defects at higher depths.

Examining these profiles in more detail, $S(E)$ in the pristine film first displays a sharp decrease in the range of 0.03 to 63 nm, followed by a gradual decay until it becomes relatively constant. Irradiation to doses of 0.006 and 0.06 dpa leads to a large increase in *S* as compared to the pristine sample and can be attributed to the formation

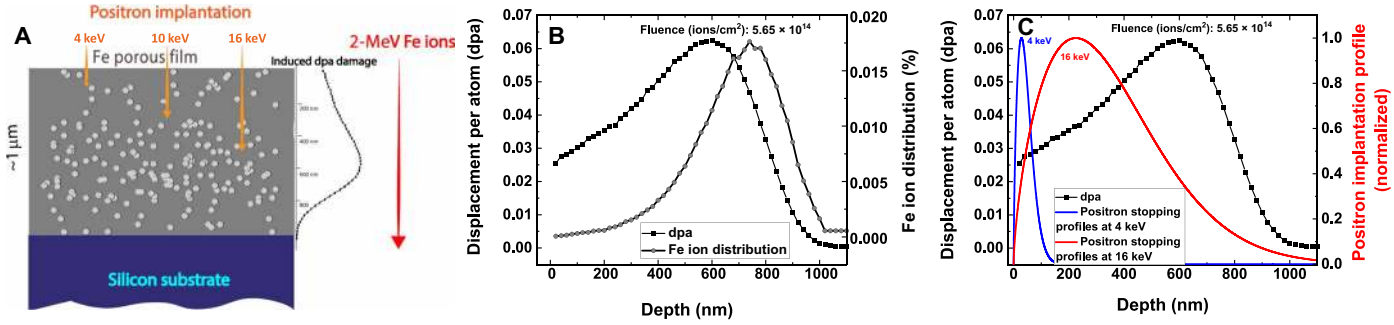

Fig. 2. Damage and positron implantation profiles in the Fe thin films. (**A**) Schematic illustrating the range of Fe ions in the film, the induced dpa damage profile, the formation of irradiation-induced defects, and the implantation of the positron beam with variable energies. (**B**) Damage profile as generated from SRIM simulations as a function of depth. Irradiation was performed using 2-MeV Fe ions. (**C**) Overlap of the damage profile in Fe when irradiated with 2-MeV Fe ions, as simulated by SRIM, and a Makhovian distribution profile of positrons at implantation energies of 4 and 16 keV, respectively. Positrons implanted at 16 keV show a large increase in the overlap with the radiation damage profile compared to those implanted at lower energies, providing a depth-dependent interaction with the damage.

of small vacancy clusters (as opposed to large voids, which are present in the pristine material and are less effective positron traps), which become the dominant positron traps. Irradiated samples exhibit an increase in *S* parameter within the first few kilo–electron volts of implanted positrons, which could be due to back-diffusion of positrons and their annihilation at the surface, as often observed in these materials (*30*). The *S*(*E*) profiles shown for the two irradiated samples suggest different defect characteristics with the variation of radiation dose. The sample irradiated at 0.06 dpa exhibits a sharp rise in the *S* parameter between 0.4 and 44 nm, followed by a modest change until it reaches a plateau at higher implantation depths. In addition, the *S* values are relatively larger for the 0.06 dpa–irradiated sample than the 0.006 dpa sample in the range of 0.05 to 63 nm, indicating that more radiation-induced defects have been introduced at the surface region with the increased dose. At greater depths, *S* is smaller for 0.06 dpa than for 0.006 dpa, perhaps because of the growth of some vacancy clusters to larger voids that are not strong positron traps. This will be examined in detail below in conjunction with positron lifetime data.

Figure 3A also shows fits of the *S*(*E*) profiles, as obtained from VEPFIT (*29*), from which the average positron diffusion lengths (L_+) within the three samples can be obtained, as summarized in the table (Fig. 3B). L_+ in the pristine sample is notably lower than that calculated for defect-free iron (see Materials and Methods) and is expected for a reference film with a high concentration of defects before irradiation, consistent with the TEM analysis discussed below, which provide higher-magnification imaging than in Fig. 1 for quantitative analysis of the initial void density. The uncertainties in the fitted L_+ are comparable to those reported in the literature (*31*). As defect densities increase, positron scattering and trapping rates increase, which result in shorter diffusion lengths. This can be observed here, with the irradiated samples exhibiting smaller L_+ values than the reference sample. L_+ for the 0.06 dpa–irradiated sample features higher uncertainty; however, given that the uncertainty is less than the magnitude, it can still provide reasonable bounds on the defect concentration (*32*). In principle, a substantial increase in irradiation dose would notably change the defect distribution and densities and typically lowers the positron diffusion length. This is also well supported by the PAS data, as when the irradiation dose was increased by a factor of 10 from 0.006 to 0.06 dpa, the *S*(*E*) profiles showed remarkable differences throughout the depth. Similarly, a sharp increase in the PALS parameters, including individual positron lifetime components and average lifetime values, was observed. These experimental observations and trends are well reflected when lower bounds of the positron diffusion lengths are taken. This also allows for the estimation of an upper bound on the defect concentration and reduces the magnitude of uncertainties associated with the calculation of the average values of defect densities due to the large spread of diffusion length at higher dpa dose.

Depth-resolved PALS measurements

PALS has been established as the key tool to determine the size and nature of open volume and vacancy-related defects (*33*). However, as noted, its application to ion-irradiated materials was not possible because of the absence of pulsed positron beams. Here, we use a monoenergetic pulsed positron beam with controlled implantation energy (and thus penetration depth) to probe the subsurface region of the ion-irradiated films from a few to hundreds of nanometers. At each depth, we collect a positron lifetime spectrum (Fig. 3B shows a representative lifetime spectrum with two components) and analyze it as explained in Materials and Methods. Positrons at each depth annihilate with electrons either from a delocalized state in the bulk or from a trapped state in a vacancy cluster. When no trap is present, the positrons annihilate in the bulk with only one lifetime equal to the bulk lifetime (τ_b), which is well known for most materials (*11*, *34*). When vacancy clusters are present, they strongly trap positrons, delaying annihilation and leading to longer lifetimes due to the lower electron density inside vacancies. It is worth noting that positrons are typically sensitive to trapping at vacancy centers having concentrations as low as 0.1 ppm (parts per million) (*11*). Fitting the lifetime spectrum often gives two or three lifetime components with their intensities, depending on the number of traps and the feasibility of resolving their lifetimes. The lifetime value and intensity are related to the size and density of vacancy clusters, respectively. The lifetime values for vacancy clusters in Fe up to 15 vacancies are known from density functional theory calculations (*34*) and will be used here for data interpretation. It should be mentioned here that grain boundaries should not affect positron trapping or diffusion in large-grained materials as are present in the current study.

Fitting the spectra of all samples gave two components (τ_1 and τ_2; Fig. 3D) and their intensities (I_1 and I_2; Fig. 3E) for each sample; Figure 3F shows the average lifetime value (see Materials and Methods).

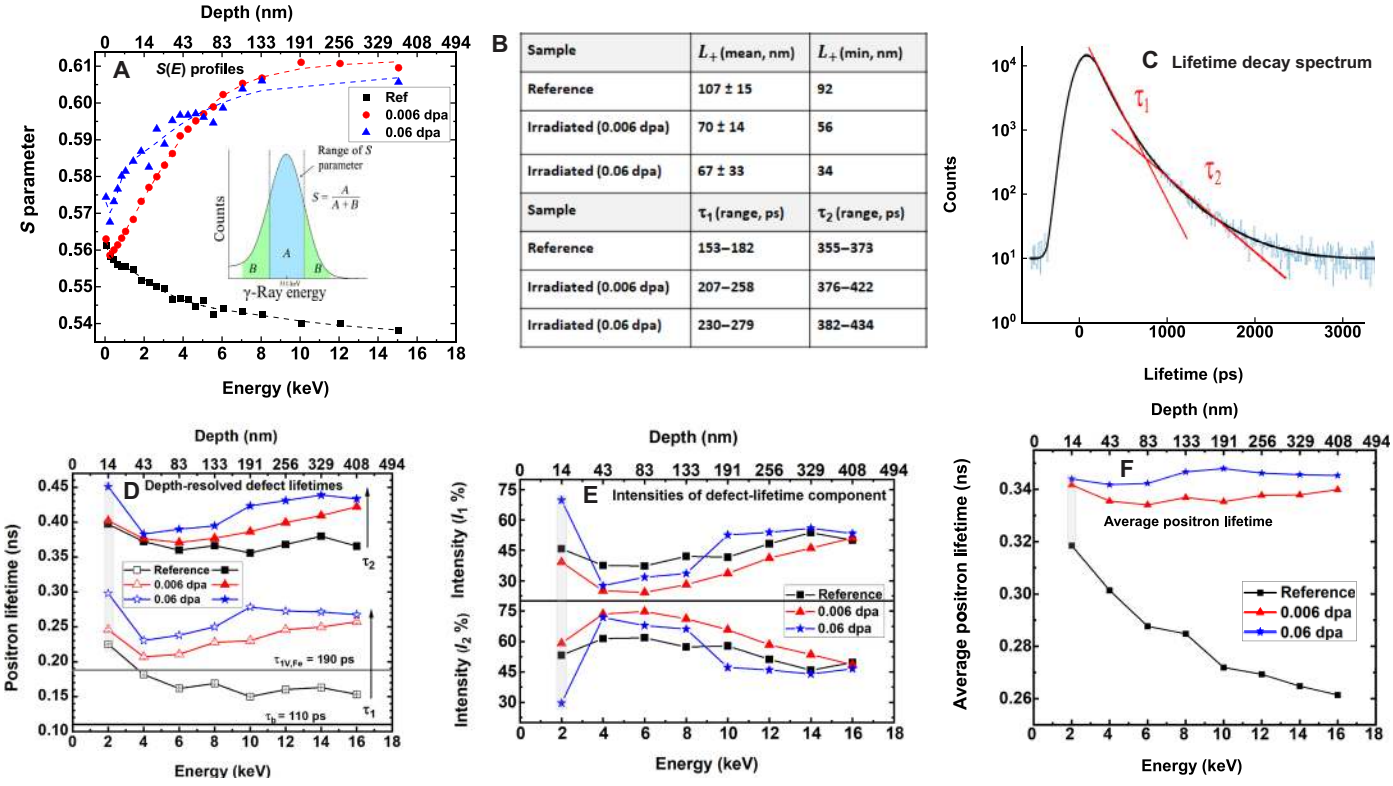

Sample	L_+ (mean, nm)	L_+ (min, nm)
Reference	107 ± 15	92
Irradiated (0.006 dpa)	70 ± 14	56
Irradiated (0.06 dpa)	67 ± 33	34
Sample	**τ_1 (range, ps)**	**τ_2 (range, ps)**
Reference	153–182	355–373
Irradiated (0.006 dpa)	207–258	376–422
Irradiated (0.06 dpa)	230–279	382–434

Fig. 3. Summary of PAS results. (**A**) DBS measurements for the Fe films featuring defect parameter *S* as a function of positron implantation energy (*E*) and depth. Dashed lines represent fits of *S*(*E*) profiles by VEPFIT. The inset shows calculations of *S* from the 511-keV peak at every energy. (**B**) Table of L_+ values (average positron diffusion length) and the two lifetime components τ_1 and τ_2 for each sample. (**C**) Visual representation illustrating how a lifetime spectrum is decomposed to τ_1 and τ_2. (**D** to **F**) PALS measurements of Fe films as a function of *E* (bottom *X* axis) and mean depth (top *X* axis) before and after irradiation: (D) Lifetime components τ_1 and τ_2 corresponding to the two different defect groups. The known bulk and monovacancy lifetimes (*42*) are marked as horizontal lines. (E) Corresponding intensity components I_1 and I_2. (F) Average lifetime values. The gray area marked at 2 keV indicates values obtained at the surface; their reliability cannot be ascertained as they could have high contributions from positron trapping at the surface. Results for this region are not considered further in this work. All error bars are smaller than the dimensions of the symbols in the figures.

[More details about the fitting and applying the two-defect trapping model (*21*) are discussed in the next section in conjunction with defect density calculations.] The short-lived components (τ_1) in all samples exhibit lifetimes higher than the previously reported bulk value τ_b in the range of 106 to 110 ps for Fe (*15*, *25*); the upper limit is considered in this study. This indicates that all positrons were trapped at defects and that no positron annihilation occurs in the bulk even in the reference sample, another indicator of the high density of defects in the starting material, as shown in Fig. 1. Accordingly, the two fitted lifetimes τ_1 and τ_2 represent two defect groups. The observed increase in the lifetime values when the material is subjected to radiation, in the order of 0.06 dpa > 0.006 dpa > reference, is indicative of the growth in the size of vacancy clusters with increasing dose. In the reference film, τ_1 is within the 153- to 182-ps range, which is higher than τ_b (110 ps) and lower than the monovacancy lifetime τ_{1V} (175 to 190 ps) for Fe (*34*, *35*); again, the upper limit is considered in this study. Such lifetime values are known to be associated with dislocations (*34*, *35*). The second lifetime τ_2 in the pristine film is around 350 ps, indicating the presence of large clusters containing about 10 vacancies (10 V). In the irradiated samples, the first lifetime component τ_1 exhibits values ranging from 207 to 258 ps, indicating the presence of divacancies (2 V) in the lower-dose sample that grow to small vacancy clusters pertaining to the size of four vacancies (4 V) when the dose is increased to 0.06 dpa. A similar trend is observed for the second lifetime τ_2 where the sample irradiated to 0.06 dpa has higher long-lived lifetimes (ranging from 382 to 434 ps) as compared to the lower-dose sample (376 to 422 ps). These values indicate the formation of clusters containing more than 15 vacancies (15 V) (*34*).

Defect density calculations

Standard trapping models can be applied to calculate the defect densities where the trapping rate (*K*) is proportional to the defect concentration (*C*), where the proportionality constant is given by a defect-specific positron trapping coefficient μ (see Materials and Methods)

$$K = \mu C \quad (1)$$

The standard two-defect trapping model (*36*) assumes two defect groups and is often applied to decompose lifetime spectra into a sum of three exponentials. The first is a bulk-like component with reduced lifetime (τ_0) compared to the bulk defect-free lattice (τ_b) because the presence of defects scatters positrons and limits their diffusion and lifetimes. The other two components exhibit extended lifetimes corresponding to two different positron trapping centers. However, when large concentrations of defects are present in the samples, nearly all the positrons become trapped at defects and no

annihilation signal arises from the bulk. In this case, τ_0 becomes negligible, and only two lifetime components are observed, both of which can be treated as defect lifetimes. As explained above, the samples used in this work contain a large concentration of defects with only two lifetime values sufficiently higher than that of bulk lattice. Thus, because we do not observe τ_0 in the measurements, we treat the two components τ_1 and τ_2 as defect-specific lifetimes with relative intensities I_1 and I_2 corresponding to two groups of defects. As per the lifetime data shown in Fig. 3D, the first group of defects (D_1) can be assigned to relatively shallow positron traps (associated with 153- to 182-ps lifetimes) such as dislocations or small vacancy clusters (associated with lifetimes greater than 190 ps), while the second group of defects (D_2) is assigned to large vacancy clusters extending to 15 V (*34*). There is a considerable increase in the lifetime, i.e., in the cluster size, around 190 nm for the higher dose, which is a result of the depth distribution of the 2-MeV Fe ions used for irradiation.

Because we have saturated positron trapping at defects, the standard method for calculating trapping rates from PALS is not applicable. Instead, we calculate the trapping rate from L_+ and combine both variable energy DBS and PALS to yield an effective method for a meticulous assessment of depth-resolved defect densities even in highly defected films. More details are presented in Materials and Methods. Figure 4A displays the trapping rates as a function of depth. The calculated defect densities corresponding to the two defect groups are provided in Fig. 4 (B to D). The dislocation density in the pristine film calculated from PAS measurements using this analysis (presented in Fig. 4B) is in very good agreement with the TEM measurements in Fig. 1B.

In accordance with the lifetime data provided above, the defect densities corresponding to both defect groups consisting of small-sized point defects (Fig. 4C) and large clusters (Fig. 4D) increase considerably when the material is irradiated to 0.006 dpa and displayed a further increase when the dose was elevated one order of magnitude to 0.06 dpa. The density of small clusters increases with depth, while it decreases for larger clusters at high depths. This is also reflected in the depth dependence of the ratio between the density of large clusters and small clusters (Fig. 4E). The decrease in the density of group D_2 defects (which represents large clusters >15 vacancies) with depth (Fig. 4D) is associated with an increase in their size as indicated from the increase in lifetime in Fig. 3C, which is a direct result of the increase in cluster size. This implies that these defects have agglomerated to form larger clusters and reveals that larger clusters are stable at higher penetration depths away from the surface. No monovacancies were detected as they are often highly mobile

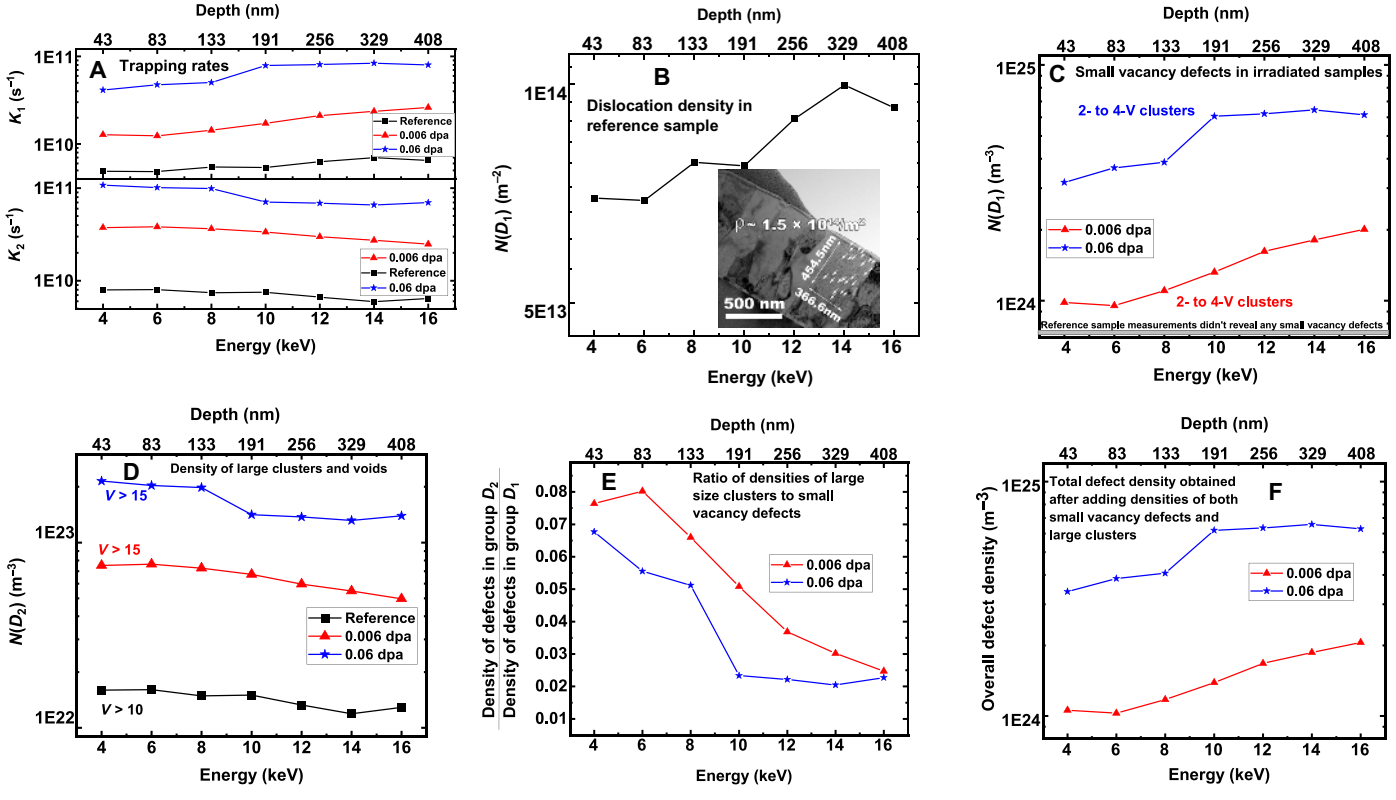

Fig. 4. Properties of ion beam–induced defects in the thin films from PAS. (**A** and **B**) Calculations of defect parameters for reference and irradiated samples as a function of implantation energy and depth, featuring (A) trapping rates obtained from positron diffusion lengths and Eq. 3 and (B) dislocation densities (m^{-2}), $N(D_1)$, calculated for the reference sample. The inset of the figure shows a TEM micrograph taken from Fig. 1 featuring the dislocation density as measured from that micrograph. Note the high density of dislocations, consistent with the TEM results in Fig. 1. (**C**) Densities of small clusters (m^{-3}), $N(D_1)$, determined for ion-irradiated samples corresponding to defect group D_1. (**D**) Densities of larger clusters (m^{-3}), $N(D_2)$, determined for both the reference and ion-irradiated samples, corresponding to defect group D_2. (**E**) Ratio of defect densities calculated for irradiated samples corresponding to the two defect groups D_1 and D_2. This ratio illustrates agglomeration of vacancy clusters; it decreases with the formation of large vacancy clusters at higher depths and higher dose. (**F**) Overall defect density obtained for irradiated samples by summation of individual defect densities corresponding to defect groups D_1 and D_2. All samples exhibited very high defect concentrations.

unless trapped at impurities, which is not the case in the current measurements, possibly because of lower impurity concentrations or the high density of sinks in the films.

TEM data and calculation of cavity and void density

The microstructures of the higher-dose irradiated films were directly observed with TEM bright-field (BF) imaging following irradiation (Fig. 5). The cavity density and average cavity size for the pristine sample and the sample irradiated to 0.06 dpa are presented in Fig. 5 (A and B). The cavity density is on the order of 1×10^{23} m^{-3} for the two samples. That is, the density did not change substantially upon irradiation. For the reference case, the average cavity size ranges from 1.8 to 2.0 nm and shows a dependence on depth, while it ranges from 1.6 to 2.0 nm for the sample irradiated to 0.06 dpa and shows a stronger dependence on depth. The cavity size for the irradiated sample was measured to be 1.94 nm at a depth of 130 nm and decreased to 1.61 nm at a depth of 340 nm.

The TEM observations show that the cavity density, already very high in the pristine film, is unchanged to a dose of 0.06 dpa. However, the average cavity size decreased after irradiation. At the same time, the PAS results showed an increase in the density and size of smaller defect clusters with irradiation. This suggests that irradiation is shrinking the larger-scale TEM-visible cavities present in the samples while simultaneously creating and growing the smaller-scale vacancy clusters that can be observed by PAS. The data here reveal that void shrinking can happen at least for irradiation dose below 0.1 dpa. Further studies are needed to illustrate whether this

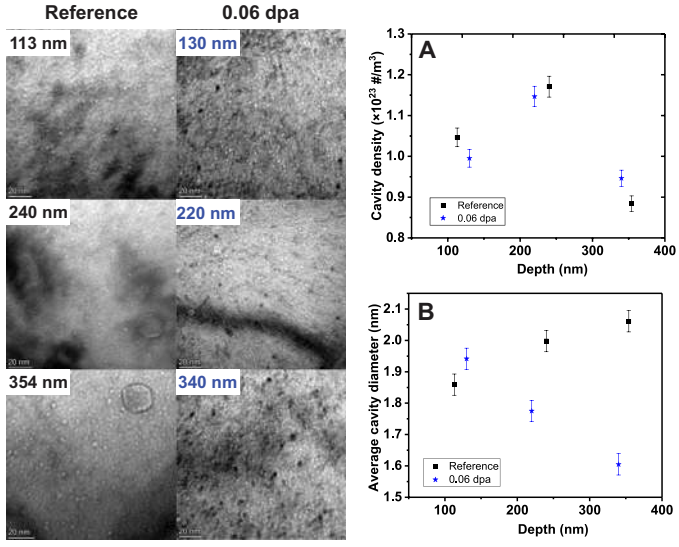

Fig. 5. Post-irradiation microstructure of the Fe films. Defect quantification from TEM micrographs of the irradiated sample showing (**A**) cavity density and (**B**) average cavity size plotted as a function of depth from the surface. Figures to the left of the plots show the micrographs used for the cavity calculations for both the pristine and 0.06-dpa samples. The numbers on the figure indicate the depth at which the TEM sample was lifted out in the film (they are thus the exact abscissa of the data plotted on the right).

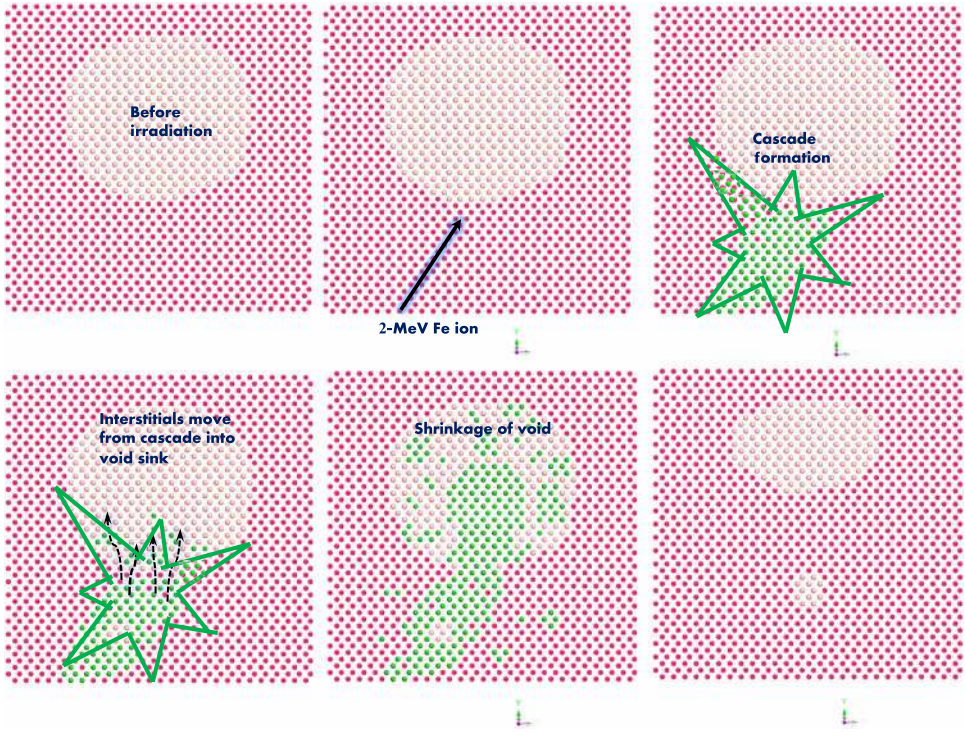

Fig. 6. New mechanism revealed by this study. The schematic shows the preexisting voids in the reference films and the overlap between them and the cascade induced by irradiation. As they interact, interstitials produced from the cascade flow to the preexisting voids, which act as sinks for interstitials, causing the voids to shrink. Because of reduced in-cascade annihilation, larger numbers of small vacancy clusters are produced in the center of the cascade than would be produced if the voids were not present. This mechanism highlights the competing effects of sinks in the material. On the one hand, they eliminate interstitials produced under irradiation. On the other hand, they exacerbate the formation of vacancy defects.

behavior would last at higher doses. The aforementioned interpretation is supported by recent work by Fellman *et al*. (*37*) who simulated voids and other vacancy-type defects interacting with cascade events induced by irradiation in body-centered cubic (BCC) tungsten at room temperature. They observed that cascades overlapping with preexisting voids resulted in a notable decrease in the original void size. In these simulations, not only did preexisting voids decrease in size but new vacancy clusters survived after cascade overlap. Our combined PAS and TEM results demonstrate a very similar behavior in highly defective Fe films, a direct experimental validation of the modeling results. Because of the high initial cavity density in the reference films in our study, the probability of cascade overlapping with preexisting cavities is high, leading to a reduction in the void size and a corresponding increase in the surviving vacancies after cascade events, due to the sink behavior of the voids with cascade-produced interstitials. This mechanism is schematically illustrated in Fig. 6. The surviving vacancies form smaller vacancy-cluster defects that are too small for TEM to image but are detected by PAS. Thus, by combining PAS with TEM on ion-irradiated materials, new insight into the evolution of radiation damage has been revealed.

This work shows the effectiveness of PAS in quantifying the size distribution and concentrations of vacancy clusters associated with ion irradiation. The recent development of pulsed positron beams with good timing resolution provides a new capability for applying PALS on ion-irradiated samples. Future studies of defect formation in magnetic materials such as iron could also greatly benefit from the development of spin-polarized positron beams.

PALS, combined with more traditional TEM observations, reveals an important new mechanism for cascade-void interaction, where cascade formation leads to shrinkage in the size of preexisting voids associated with an enhancement in the formation of smaller vacancy clusters. These results provide direct evidence of the ability of internal surfaces to act as sinks for defects (*38*), providing at least a temporary reduction in the growth of larger-scale defects responsible for material failure. They also demonstrate the ability to nondestructively probe the damage produced during ion irradiation, opening the way for new types of radiation damage studies and more direct validation of modeling and simulations.

MATERIALS AND METHODS

Material growth and preparation

Coarse-grained films were grown at 500°C on Si (100) substrates using the physical vapor deposition system at the Center for Integrated Nanotechnologies (CINT) at the Los Alamos National Laboratory. Before deposition, the high-vacuum growth chamber reached a base pressure of $\leq 5.0 \times 10^{-8}$ torr. An Fe source, running at a power of 400 W, was used to provide Fe atoms. The deposition rate was approximately 0.2 to 0.3 nm/s, with the total time of the deposition being 4000 s.

Ion irradiation

Ion irradiation of the Fe films was performed with 2-MeV Fe ions at room temperature on the 3-MV tandem accelerator at the Ion Beam Materials Laboratory at the Los Alamos National Laboratory. To achieve 1 cm in diameter irradiation area, which is needed for PAS characterization, the focused 2-MeV Fe ion beam was rastered using an electrostatic scanner with fixed frequencies of 512 and 64 Hz in horizontal and vertical directions, respectively. The ion fluence was measured using a four-corner Faraday cup assembly in front of the samples. The target chamber vacuum was maintained below 5×10^{-8} torr during all irradiations. Irradiations with a peak damage of 0.006 to 0.06 dpa were carried out using a fixed damage rate of approximately 2.5×10^{-4} dpa/s. The beam fluence to damage conversion was based on SRIM Monte Carlo code simulations using the *K-P* mode with a displacement threshold energy of 40 eV for all the elements involved.

Transmission electron microscopy

TEM measurements were carried out to investigate the microstructure of both the reference and irradiated samples, revealing that the reference films are highly defected with a high density of dislocations and loops, as shown in Fig. 1. Cross-sectional TEM samples were prepared from the deposited Fe films by the focused ion beam (FIB) lift-out method. The lift-outs were created with a FEI Quanta 3D FEG Dual Beam SEM/FIB, with a Ga ion source capable of energies up to 30 kV. Final thinning was done at 2 keV to reduce the Ga beam damage before examination in the TEM. After preparation, the TEM samples were imaged using both a JEOL JEM-ARM200CF and FEI Talos F200X G2 analytical for the unirradiated samples. For the irradiated samples, the JEOL ARM200CF was used in TEM mode to measure the defect distribution, with images taken using a Gatan Orius SC200D camera and the Gatan Microscopy Suite v3.3. TEM BF images were acquired at under- and over-focused conditions with a defocus value of 2.36 μm to observe the cavities present in the samples. The under-focused images were selected to measure the size and density of the cavities. In the under-focused TEM images, cavities appear predominantly as white circles encircled by a darker Fresnel fringe. The cavity size was measured as the inner diameter of the dark fringe surrounding the white dots (*39*).

Variable energy positron annihilation spectroscopy

VEPAS was performed at the positron facility at the Helmholtz-Zentrum Dresden-Rossendorf (HZDR) in Dresden, Germany (*17*, *21*). DBS measurements were carried out at room temperature for each sample in the range of 0.05 to 16 keV using a DC monoenergetic positron beam. A high-purity Ge detector was used to detect 511-keV γ rays produced by positron annihilation at each beam energy with an energy resolution of 1.09 ± 0.01 keV at 511 keV. The resulting spectra were characterized by line-shape parameter *S* representing annihilation events with valence (low-momentum) electrons (*11*, *13*).

Depth-resolved positron annihilation lifetime measurements were performed in the 0.5- to 16-keV range at the monoenergetic positron spectroscopy (MePS) beamline facility, also at the HZDR (*21*). The resolution function was determined to be around 250 ps, and positrons were generated with a flux of 10^6/s. MePS is one of the subsystems of EPOS (ELBE Positron Source) connected to the primary electron beam: electron linac for beams with high brilliance and low emittance (ELBE). The positron beam at MePS is created by pair production of ELBE electron beam on a tungsten target, and positrons are generated with a flux of 10^6/s. At each beam energy, spectra of more than 10^6 annihilation events were recorded. The lifetime spectra [$N(t)$] were generated by taking the time derivative of the positron decay spectrum and can be expressed in terms of individual positron lifetimes (τ_i) and corresponding intensities (I_i), as described by the equation $N(t) = \Sigma_i I_i/\tau_i \cdot \exp(-t/\tau_i)$.

A set of Gaussian distribution functions was convoluted with the obtained lifetime spectra to describe the spectrometer resolution function and was confirmed to be around 250 ps. The obtained spectra were analyzed using the PALSfit software (*40*) and were decomposed

into two lifetime components. An additional third component was found with negligible intensity (<1%) and lifetime in the range of 1 to 2 ns, which can be attributed to the formation of ortho-positronium and thus ignored.

Calculation of mean penetration depth

The mean penetration depth of positrons can be calculated from their implantation energies using the following power law (*26*): $\bar{x} = \frac{A}{\rho}E^n$, where $A = 3.6\ \mu g/cm^2\ keV^{-1.6}$ and $n = 1.6$ are independent empirical parameters (*41*) related to theoretical and experimental uncertainties, and ρ is the material density, which is 7.874 g/cm^{-3} for pure iron.

Calculation of bulk positron diffusion length L_+ (to be used in defect density calculations)

The bulk positron diffusion length (L_{+b}) within a defect-free material is given by

$$L_{+b} = \sqrt{D_+ \tau_b} \quad (2)$$

where D_+ is the positron diffusion coefficient within the bulk material and τ_b is the positron annihilation lifetime in bulk. They are equal to 1.87 $cm^2\ s^{-1}$ and 110 ps, respectively, for pure single-crystalline iron (*42*). From Eq. 2, L_{+b} in iron is estimated to be around 143.42 nm.

L_+ values for the three samples were obtained from fitting the $S(E)$ curve using VEPFIT as explained in Results. The VEPFIT program, introduced by van Veen *et al.* (*29*), features a calculation routine based on the solution for the time-averaged positron density equation. The software follows a semilinear fitting regime where a multistep procedure is followed by solving a linear minimization problem using the least-squares approach at every step of the nonlinear iteration. The *S* parameters (including bulk, defect, surface, and epithermal) are input as linear parameters, which are then used to solve for the calculation of nonlinear parameters like diffusion lengths and layer ranges. All the samples were fitted according to "Model 4," which features calculations for layered structures of defects in materials (*29*). The fitting required a two-layered model featuring a surface layer and nonsurface region of the film. The fitting determined the width of the surface layer to be less than 40 nm for all the samples, and the corresponding L_+ values were found to be around 16(1) nm for the reference sample, 11(1) nm for the 0.006 dpa–irradiated sample, and 8(0.6) nm for the 0.06 dpa–irradiated sample. These low L_+ values in layer 1 are attributed to the high density of defects at surface. The L_+ values corresponding to the nonsurface layer of the film are depicted in Fig. 3B for all the samples. In addition, the reference and 0.006 dpa–irradiated samples exhibited relatively good fits (reduced χ^2 around 1.7 and 1.5, respectively) as compared to the 0.06 dpa–irradiated film (reduced χ^2 around 9). In principle, L_+ values are discerned from the diffusion of positrons, implanted at low energy, back to the surface, where annihilation occurs at defect-like surface states. From Fig. 3A, it is clear that the sample irradiated at 0.06 dpa has markedly higher *S* values at the surface (0.4 to 44 nm), which implies that the 0.06 dpa–irradiated sample should manifest shorter diffusion length. This implies that the 0.06 dpa sample has a higher defect concentration. However, it is difficult to conclude this with the mean fit values observed for irradiated samples. Thus, using the lower bounds (given by average value minus standard deviation) of the fitted diffusion lengths yields an estimated upper bound on the defect concentrations, which is consistent with the PALS data acquired for these samples, where both the fitted defect lifetimes and the average lifetime exhibit higher values in the 0.06 dpa sample than the 0.006 dpa sample, demonstrating higher concentration of defects as expected. This suggests that a value closer to the lower bound of L_+ better represents the defect concentration. Thus, the positron trapping rates and defect densities are calculated using the lower limits of fitted diffusion lengths.

Calculation of depth-resolved defect densities

Because, as discussed, the entirety of the positron annihilation signals is generated from defects in these samples, the conventional approach for calculating the trapping rates from lifetime measurements using the standard trapping model is not applicable. Instead, we calculate positron trapping rates from the positron diffusion length obtained from the DBS measurements. It is well known that positron diffusion lengths derived from back diffusion of implanted positrons can still provide an accurate estimation of defect density even in the case of saturation trapping (*32*, *43*). For this analysis, the total trapping rate of defects in each film can thus be given by

$$K = \frac{1}{\tau_b}\left(\frac{L_{+b}^2}{L_+^2} - 1\right) \quad (3)$$

The value of the trapping rate obtained from Eq. 3 is an average value containing the combined contributions of defects present in both groups D_1 and D_2 measured by PALS and therefore can be decomposed into individual components by using values of the intensities obtained from positron lifetime experiments (*43*), as given by the following equation

$$K_i = I_i K \quad (4)$$

where K_i ($i = 1$ and 2) are the individual trapping rates corresponding to the intensity component from each defect group at a given implantation depth and are represented in Fig. 4A. Note that *K* is the total trapping rate calculated from Eq. 3 for each sample.

As discussed above, the concentration of defects can then be directly obtained from Eq. 1 by using the defect-specific positron trapping coefficient as a constant of proportionality assuming it to be relatively constant within one defect group. In the literature, the typical specific trapping coefficient value used for the Fe monovacancy is $1.3 \times 10^{-14}\ m^3\ s^{-1}$ (*33*, *44*), while for large vacancy clusters in Cu, a value on the order of $5 \times 10^{-13}\ m^3\ s^{-1}$ was reported (*45*), which has been successfully applied in previous reports (*33*) for calculations of vacancy clusters in iron and thus will be applied here for the calculation of defect density. For the reference sample, where the lifetime values obtained in group D_1 are less than that of monovacancies, the value for the specific trapping coefficient used is for Fe dislocation loops, assumed to be $7 \times 10^{-5}\ m^2\ s^{-1}$, as previously reported (*45*). Last, it should be mentioned that the accuracy of the defect density calculations is limited by the unavailability of positron trapping coefficients for all cluster sizes. They have only been reported for single vacancies, dislocations, and large clusters.

REFERENCES AND NOTES

1. A. B. Adewoye, S. J. Lindsay, Y. E. Dubrova, M. E. Hurles, The genome-wide effects of ionizing radiation on mutation induction in the mammalian germline. *Nat. Commun.* **6**, 6684 (2015).
2. C. L. Tracy, M. Lang, J. M. Pray, F. Zhang, D. Popov, C. Park, C. Trautmann, M. Bender, D. Severin, V. A. Skuratov, R. C. Ewing, Redox response of actinide materials to highly ionizing radiation. *Nat. Commun.* **6**, 6133 (2015).

3. F. Granberg, K. Nordlund, M. W. Ullah, K. Jin, C. Lu, H. Bei, L. M. Wang, F. Djurabekova, W. J. Weber, Y. Zhang, Mechanism of radiation damage reduction in equiatomic multicomponent single phase alloys. *Phys. Rev. Lett.* **116**, 135504 (2016).
4. J. Knaster, A. Moeslang, T. Muroga, Materials research for fusion. *Nat. Phys.* **12**, 424–434 (2016).
5. M. B. Agranat, O. V. Chefonov, A. V. Ovchinnikov, S. I. Ashitkov, V. E. Fortov, P. S. Kondratenko, Damage in a thin metal film by high-power Terahertz radiation. *Phys. Rev. Lett.* **120**, 085704 (2018).
6. W. Han, M. J. Demkowicz, N. A. Mara, E. Fu, S. Sinha, A. D. Rollett, Y. Wang, J. S. Carpenter, I. J. Beyerlein, A. Misra, Design of radiation tolerant materials via interface engineering. *Adv. Mater.* **25**, 6975–6979 (2013).
7. X. Yi, M. L. Jenkins, K. Hattar, P. D. Edmondson, S. G. Roberts, Characterisation of radiation damage in W and W-based alloys from 2 MeV self-ion near-bulk implantations. *Acta Mater.* **92**, 163–177 (2015).
8. C. Liu, L. He, Y. Zhai, B. Tyburska-Püschel, P. M. Voyles, K. Sridharan, D. Morgan, I. Szlufarska, Evolution of small defect clusters in ion-irradiated 3C-SiC: Combined cluster dynamics modeling and experimental study. *Acta Mater.* **125**, 377–389 (2017).
9. C. Heintze, F. Bergner, M. Hernández-Mayoral, R. Kögler, G. Müller, A. Ulbricht, Irradiation hardening of Fe–9Cr-based alloys and ODS Eurofer: Effect of helium implantation and iron-ion irradiation at 300 °C including sequence effects. *J. Nucl. Mater.* **470**, 258–267 (2016).
10. F. A. Selim, M. H. Weber, D. Solodovnikov, K. G. Lynn, Nature of native defects in ZnO. *Phys. Rev. Lett.* **99**, 085502 (2007).
11. R. Krause-Rehberg, H. S. Leipner, *Positron Annihilation in Semiconductors: Defect Studies* (Springer Science & Business Media, 1999).
12. K. Sraitrova, J. Cizek, V. Holy, T. Plechacek, L. Benes, M. Jarosova, V. Kucek, C. Drasar, Vacancies in SnSe single crystals in a near-equilibrium state. *Phys. Rev. B* **99**, 035306 (2019).
13. P. J. Schultz, K. G. Lynn, Interaction of positron beams with surfaces, thin films, and interfaces. *Rev. Mod. Phys.* **60**, 701–779 (1988).
14. J. Jiang, Y. C. Wu, X. B. Liu, R. S. Wang, Y. Nagai, K. Inoue, Y. Shimizu, T. Toyamac, Microstructural evolution of RPV steels under proton and ion irradiation studied by positron annihilation spectroscopy. *J. Nucl. Mater.* **458**, 326–334 (2015).
15. H. Zhu, Z. Wang, X. Gao, M. Cui, B. Li, J. Sun, C. Yao, K. Wei, T. Shen, L. Pang, Y. Zhu, Y. Li, J. Wang, P. Song, P. Zhang, X. Cao, Positron annihilation Doppler broadening spectroscopy study on Fe-ion irradiated NHS steel. *Nucl. Instrum. Methods Phys. Res. Sect. B* **344**, 5–10 (2015).
16. S. Saini, R. Menon, S. K. Sharma, A. P. Srivastava, S. Mukherjee, P. Y. Nabhiraj, P. K. Pujari, D. Srivastava, G. K. Dey, Ar irradiated Cr rich Ni alloy studied using positron annihilation spectroscopy. *J. Nucl. Mater.* **479**, 279–286 (2016).
17. M. O. Liedke, W. Anwand, R. Bali, S. Cornelius, M. Butterling, T. T. Trinh, A. Wagner, S. Salamon, D. Walecki, A. Smekhova, H. Wende, K. Potzger, Open volume defects and magnetic phase transition in $Fe_{60}Al_{40}$ transition metal aluminide. *J. Appl. Phys.* **117**, 163908 (2015).
18. M. Reiner, T. Gigl, R. Jany, G. Hammerl, C. Hugenschmidt, Impact of oxygen diffusion on superconductivity in $YBa_2Cu_3O_{7-\delta}$ thin films studied by positron annihilation spectroscopy. *Phys. Rev. B* **97**, 144503 (2018).
19. W. Egger, P. Sperr, G. Kögel, G. Dollinger, Pulsed low energy positron system (PLEPS) at the Munich research reactor FRM II. *Phys. Stat. Solidi C* **4**, 3969–3972 (2007).
20. K. Ito, Preliminary results on low-energy positron age-momentum correlation measurements based on a radioisotope-source positron beam. *JJAP Conf. Proc.* **7**, 011302 (2018).
21. A. Wagner, M. Butterling, M. O. Liedke, K. Potzger, R. Krause-Rehberg, Positron annihilation lifetime and Doppler broadening spectroscopy at the ELBE facility. *AIP Conf. Proc.* **1970**, 040003 (2018).
22. V. Sabelová, V. Kršjak, J. Kuriplach, M. Petriska, V. Slugeň, J. Š. Veterníková, Characterization of helium implanted Fe–Cr alloys by means of positron annihilation methods. *J. Nucl. Mater.* **450**, 54–58 (2014).
23. V. Krsjak, J. Kuriplach, C. Vieh, L. Peng, Y. Dai, On the empirical determination of positron trapping coefficient at nano-scale helium bubbles in steels irradiated in spallation target. *J. Nucl. Mater.* **504**, 277–280 (2018).
24. V. Krsjak, J. Degmova, S. Sojak, V. Slugen, Effects of displacement damage and helium production rates on the nucleation and growth of helium bubbles – Positron annihilation spectroscopy aspects. *J. Nucl. Mater.* **499**, 38–46 (2018).
25. P. Horodek, J. Dryzek, V. A. Skuratov, Studies of iron exposed to heavy ion implantation using positron annihilation spectroscopy. *Radiat. Phys. Chem.* **122**, 60–65 (2016).
26. P. Asoka-Kumar, K. G. Lynn, Implantation profile of low-energy positrons in solids. *Appl. Phys. Lett.* **57**, 1634–1636 (1990).
27. F. A. Selim, D. Winarski, C. R. Varney, M. C. Tarun, J. Ji, M. D. McCluskey, Generation and characterization of point defects in $SrTiO_3$ and $Y_3Al_5O_{12}$. *Results Phys.* **5**, 28–31 (2015).
28. F. A. Selim, C. R. Varney, M. C. Tarun, M. C. Rowe, G. S. Collins, M. D. McCluskey, Positron lifetime measurements of hydrogen passivation of cation vacancies in yttrium aluminum oxide garnets. *Phys. Rev. B* **88**, 174102 (2013).
29. A. van Veen, H. Schut, J. Vries, R. A. Hakvoort, M. R. Ijpma, Analysis of positron profiling data by means of "VEPFIT". *AIP Conf. Proc.* **218**, 171 (1991).
30. P. Parente, T. Leguey, V. de Castro, T. Gigl, M. Reiner, C. Hugenschmidt, R. Pareja, Characterization of ion-irradiated ODS Fe–Cr alloys by doppler broadening spectroscopy using a positron beam. *J. Nucl. Mater.* **464**, 140–146 (2015).
31. W.-S. Hung, C.-H. Lo, M.-L. Cheng, H. Chen, G. Liu, L. Chakka, D. Nanda, K.-L. Tung, S.-H. Huang, K.-R. Lee, J.-Y. Lai, Y.-M. Sun, C.-C. Yu, R. Zhang, Y. C. Jean, Polymeric membrane studied using slow positron beam. *Appl. Surf. Sci.* **255**, 201–204 (2008).
32. J. Čížek, F. Lukáč, I. Procházka, R. Kužel, Y. Jirásková, D. Janičkovič, W. Anwand, G. Brauer, Characterization of quenched-in vacancies in Fe–Al alloys. *Phys. B Condens. Matter* **407**, 2659–2664 (2012).
33. V. Krsjak, J. Kuriplach, T. Shen, V. Sabelova, K. Sato, Y. Dai, Helium behavior in ferritic/martensitic steels irradiated in spallation target. *J. Nucl. Mater.* **456**, 382–388 (2015).
34. M. J. Puska, R. M. Nieminen, Defect spectroscopy with positrons: A general calculational method. *J. Phys. F* **13**, 333–346 (1983).
35. K. M. Mostafa, J. De Baerdemaeker, P. R. Calvillo, N. Van Caenegem, Y. Houbaert, D. Segers, A study of defects in iron based alloys by positron annihilation techniques. *Acta Phys. Pol. Ser. A* **113**, 1471–1478 (2008).
36. A. Vehanen, P. Hautojärvi, J. Johansson, J. Yli-Kauppila, P. Moser, Vacancies and carbon impurities in α- iron: Electron irradiation. *Phys. Rev. B* **25**, 762–780 (1982).
37. A. Fellman, A. E. Sand, J. Byggmästar, K. Nordlund, Radiation damage in tungsten from cascade overlap with voids and vacancy clusters. *J. Phys. Condens. Matter* **31**, 405402 (2019).
38. E. M. Bringa, D. Monk, A. Caro, A. Misra, L. Zepeda-Ruiz, M. Duchaineau, F. Abraham, M. Nastasi, S. T. Picraux, Y. Q. Wang, D. Farkas, Are nanoporous materials radiation resistant? *Nano Lett.* **12**, 3351–3355 (2011).
39. M. L. Jenkins, M. A. Kirk, *Characterisation of Radiation Damage by Transmission Electron Microscopy* (CRC Press, 2000).
40. J. V. Olsen, P. Kirkegaard, N. J. Pedersen, M. Eldrup, PALSfit: A new program for the evaluation of positron lifetime spectra. *Phys. Stat. Solidi C* **4**, 4004–4006 (2007).
41. J. Dryzek, P. Horodek, GEANT4 simulation of slow positron beam implantation profiles. *Nucl. Instrum. Methods Phys. Res. Sect. B* **266**, 4000–4009 (2008).
42. F. Lukáč, J. Čížek, I. Procházka, Y. Jirásková, D. Janičkovič, W. Anwand, G. Brauer, Vacancy-induced hardening in Fe-Al alloys. *J. Phys. Conf. Ser.* **443**, 012025 (2013).
43. R. Krause-Rehberg, V. Bondarenko, E. Thiele, R. Klemm, N. Schell, Determination of absolute defect concentrations for saturated positron trapping–deformed polycrystalline Ni as a case study. *Nucl. Instrum. Methods Phys. Res. Sect. B* **240**, 719–725 (2005).
44. M. J. Alinger, S. C. Glade, B. D. Wirth, G. R. Odette, T. Toyama, Y. Nagai, M. Hasegawa, Positron annihilation characterization of nanostructured ferritic alloys. *Mater. Sci. Eng. A* **518**, 150–157 (2009).
45. M. Eldrup, B. N. Singh, Studies of defects and defect agglomerates by positron annihilation spectroscopy. *J. Nucl. Mater.* **251**, 132–138 (1997).

Acknowledgments: This work was performed, in part, at the Analytical Instrumentation Facility (AIF) at the North Carolina State University, which is supported by the State of North Carolina and the NSF (award number ECCS-1542015). This work was performed, in part, at the CINT, an Office of Science User Facility operated for the U.S. Department of Energy (DOE) Office of Science. Los Alamos National Laboratory, an affirmative action equal opportunity employer, is managed by Triad National Security LLC for the U.S. Department of Energy's NNSA, under contract 89233218CNA000001. Parts of this research were carried out at ELBE at the HZDR e.V., a member of the Helmholtz Association. We would like to thank the facility staff for assistance. **Funding:** This work was supported as part of FUTURE (Fundamental Understanding of Transport Under Reactor Extremes), an Energy Frontier Research Center funded by the U.S. Department of Energy, Office of Science, Basic Energy Sciences. **Author contributions:** F.A.S., B.P.U., and P.H. conceived the study. B.P.U., S.A., and F.A.S. prepared and wrote the manuscript. N.L. synthesized the Fe films. Y.Q.W. irradiated the films. M.O.L., A.W., E.H., M.B., F.A.S., and Y.Q.W. performed the PAS experiments. S.A., M.O.L., E.R., A.C.L.J., and F.A.S. analyzed the PAS results. S.A. and E.R. prepared PAS graphs; J.C., N.L., D.K., and D.J.E. prepared and analyzed the TEM samples. R.A., P.H., A.A.K., L.C., D.K., and B.P.U. aided in the interpretation of the combined PAS and TEM results. All authors edited and commented on the manuscript. **Competing interests:** The authors declare that they have no competing interests. **Data and materials availability:** All data needed to evaluate the conclusions in the paper are present in the paper. Additional data related to this paper may be requested from the authors.

Submitted 10 January 2020
Accepted 16 June 2020
Published 29 July 2020
10.1126/sciadv.aba8437

Citation: S. Agarwal, M. O. Liedke, A. C. L. Jones, E. Reed, A. A. Kohnert, B. P. Uberuaga, Y. Q. Wang, J. Cooper, D. Kaoumi, N. Li, R. Auguste, P. Hosemann, L. Capolungo, D. J. Edwards, M. Butterling, E. Hirschmann, A. Wagner, F. A. Selim, A new mechanism for void-cascade interaction from nondestructive depth-resolved atomic-scale measurements of ion irradiation–induced defects in Fe. *Sci. Adv.* **6**, eaba8437 (2020).